AIAA JOURNAL
Vol. 46, No. 2, February 2008

Simulations of a Turbulent Flow Past a Sudden Expansion: A Sensitivity Analysis

C. Duwig,* M. Salewski, and L. Fuchs
Lund University, 22100 Lund, Sweden

DOI: 10.2514/1.30149

Large eddy simulation is used to study the flow behind a pair of symmetric backward-facing steps. As reported in the literature, the flow exhibits an asymmetric pattern characterized by the deflection of the jet toward one of the walls. The large eddy simulation results are compared with laser Doppler anemometry measurements showing the ability of the present numerical tool to capture the complex features of the flow. Furthermore, a sensitivity study is conducted to assess the influence of the grid resolution, the inflow boundary, the channel width, and the step size on the flowfield. The flow was found to be only weakly sensitive to the grid, assuring the quality of the simulation results. The inflow boundary influences the mean results only marginally unless low-frequency fluctuations are applied. In this case, the flowfield recovers a mean symmetry with suppression of the jet bending. The jet mean bending has also been shown to increase with the step size h and to decrease with increasing channel width.

Nomenclature

A_h	=	aspect ratio: $\Delta Z/h$
f	=	frequency
H_{channel}	=	incoming channel height
H_{comb}	=	combustor height ($H_{\text{channel}} + 2h$)
h	=	step height
R	=	expansion ratio defined as $H_{\text{comb}}/H_{\text{channel}}$
R_{UV}	=	normalized Reynolds stress component ($\langle uv\rangle - \langle u\rangle\langle v\rangle)/U_0^2$
St	=	Strouhal number, $f \cdot h/U_0$
U_0	=	bulk velocity computed in one of the inflow channels
u, v, w	=	streamwise, crosswise, and spanwise velocity components, respectively
x, y, z	=	streamwise, crosswise, and spanwise coordinates, respectively
x_R	=	length of the shorter recirculation
Δ	=	filter length
ΔZ	=	spanwise size of the domain/depth of the combustor
μ	=	dynamic viscosity
μ_Δ	=	subgrid-scale viscosity
ρ	=	density
$\langle . \rangle$	=	time-averaging operator

I. Introduction

TURBULENT flows through sudden plane expansions are common in many industrial applications ranging from mixing devices, heat exchangers, and air-conditioning systems, to mention a few examples. A better knowledge of this generic flow is required to optimize such devices. However, as pointed out by Escudier et al. [1], few studies have focused on the details of the turbulent case. One of the pioneering studies is the work of Abbot and Kline [2], who first reported measurements of the turbulent flowfield. They pointed out that two recirculation zones appear behind the steps with a central plane jet in between. However, they noticed that the middle plane symmetry is broken; that is, one of the recirculation zones is bigger than the other, as illustrated in Fig. 1. The plane jet is deflected toward one of the walls. This asymmetric flow pattern occurs when the expansion ratio R exceeds a critical value of $\sim$1.5. Further experiments have been conducted and confirmed this particular flow feature. Among them one may find Da Zilwa et al. [3], Aloui and Souhar [4], Escudier et al. [1], Besson et al. [5], and Nguyen and Bruel [6]. For a comprehensive comparative review of the available experimental data, the reader is referred to Escudier et al. [1].

Numerical simulations have also been used to study the asymmetry of the flow, in particular, in laminar cases. For example, Fuchs [7] determined the critical Reynolds number for the onset of asymmetric bifurcation for different step sizes. At higher Reynolds numbers, the flow undergoes a Hopf bifurcation. It has also been shown that as the step size increases, there is an exchange of stability between steady-symmetry breaking and the Hopf bifurcations. Drikakis [8] also performed 2D laminar computations of the bifurcation leading to the asymmetry. For higher Reynolds numbers, De Zilwa et al. [3] performed Reynolds-averaged Navier–Stokes simulations. Recently, Sugawara et al. [9] presented some large eddy simulations (LES) of a symmetric expansion plane channel. Fureby [10] also performed some LES and pointed out that the tendency of the jet to flow toward one of the walls is due to the Coanda effect. The major advantage of LES is that it allows capturing the 3D features inherent to the turbulent flow and therefore provides a better insight into the large turbulent structure dynamics.

As mentioned previously, the asymmetry of the flow appears as the expansion ratio exceeds 1.5 for turbulent flows. For low Reynolds numbers (laminar flows), it has been shown that one might sustain the flow symmetry beyond $R = 1.5$. However, flows in most practical applications are turbulent. As shown by Alleborn et al. [11], the flow exhibits a second bifurcation point, implying that the flow features become three-dimensional. This point is supported by Escudier et al. [1], who observed departures from the two-dimensionality of the averaged velocity profiles. It is also interesting to note that in the case of a jet through an axisymmetric expansion, there was a strong jet precession after the expansion, as reported by Nathan et al. [12]. For a given expansion ratio, the jet also bends after the expansion toward the outer wall of the vessel. This symmetry-breaking precession has a relatively low frequency.

Although the breaking of symmetry has been reported in several numerical and experimental studies, the sensitivity of the flow to geometry changes (e.g., spanwise width or expansion ratio) has not been established. In addition, the studies quoted previously focused mainly in time-averaged quantities but did not analyze the nature of the turbulent fluctuations in cases of large coherent structures. There is therefore a need for a detailed study and understanding of the time-

Presented as Paper 916 at the 45th AIAA Aerospace Sciences Meeting and Exhibit, Reno, NV, 8–11 January 2007; received 31 January 2007; revision received 28 August 2007; accepted for publication 7 September 2007.

*Faculty of Engineering (LTH), Division of Fluid Mechanics, Department of Energy Sciences, Box 118; Christophe.Duwig@vok.lth.se (Corresponding Author).

dependent flowfield with respect to the influence of the boundary conditions upon the results. In the present paper, we use LES for investigating the turbulence in the sudden expansion geometry used by Besson et al. [5]. First, we describe the models and numerical tools used for the study. Thereafter, a sensitivity analysis is performed to assess the influence of different parameters such as computational grid, domain size, and inflow boundary conditions. Next, the LES results are compared with the laser Doppler anemometry (LDA) measurements of Nguyen and Bruel [6]. The following sections are devoted to a sensitivity study regarding the step height and the channel width. Finally, the LES results corresponding to the base case (also studied by Nguyen and Bruel [6]) are analyzed using proper orthogonal decomposition (POD).

II. Governing Equations and Subgrid-Scale Modeling

We consider an isothermal and incompressible fluid. In the LES framework, the filtered governing equations are

$$\nabla \cdot (\bar{u}) = 0 \tag{1}$$

$$\frac{\partial \bar{u}}{\partial t} + \nabla \cdot (\bar{u}\,\bar{u}) = -\frac{1}{\rho_0}\nabla \bar{P} + \nabla \cdot \left(-\overline{uu} + \bar{u}\,\bar{u} + \frac{\mu}{\rho_0}\nabla \bar{u} \right) \tag{2}$$

where u is the velocity vector, ρ_0 is the density, μ is the viscosity, and is P the pressure. The bar denotes the spatial filtering operation.

The spatial filtering corresponds to a low-pass filter that removes the Fourier components that have a shorter length scale than the filter size. The filtering operator is linear and is assumed to be commutative with time and space derivatives. However, the filtering operation is not commutative with the nonlinear terms. Thus, nonlinear terms lead to expressions that cannot be written in terms of the filtered quantities. These terms are gathered on the right-hand side in Eq. (2) and called subgrid-scale (SGS) terms. These SGS terms must be expressed as functions of filtered quantities to close the system. The main role of the SGS terms is to account for the interaction between the resolved and the unresolved scales. In the three momentum equations, the SGS terms should account for the dissipative character of turbulence at the small (unresolved) scales, as well as for the transfer of energy among the resolved and unresolved scales.

A computational grid can only support Fourier components that have longer wavelengths than the grid size. Thus, a dependent variable that is represented on a grid that is used together with a discrete approximation for the derivatives leads to an *implicit* filtering. If no explicit SGS terms are added, then the numerical scheme should account at least for the small-scale dissipation. This is attained for any numerically stable scheme. However, too-dissipative numerical schemes are highly inappropriate for LES, because in addition to dissipation at small scales, they may also be dissipative at larger scales. This effect can be avoided by choosing appropriate (higher-order) discretizations. The technique is referred to as monotonically integrated LES (MILES) if the chosen scheme is monotonic [13,14]. In addition, the spatial resolution has to be fine enough (i.e., on the order of magnitude of the Taylor microscale). With such a resolution, the energy transfer among the scales is dissipation-independent, and therefore the numerical scheme may act implicitly as an SGS model [13,14]. One may also use nonmonotonic schemes as long as the finite difference equations are numerically stable. However, one should keep in mind that this implicit SGS or MILES approach might require a better resolution than a corresponding LES, which uses an appropriate SGS model. Nevertheless, even with explicit SGS modeling (such as the dynamic model), the spatial resolution has to be adequate.

Among appropriate (higher-order) discretizations, Grinstein and Fureby [14] advocate the use of flux-corrected transport schemes, whereas Margolin et al. [15] recommend high-order monotonicity-preserving schemes. In line with this recommendation, Duwig and Fuchs [16] used a fifth-order weighted essentially nonoscillatory (WENO) scheme that ensures numerical stability but does not significantly affect the resolved scales (i.e., low dissipation and dispersion characteristics). This scheme is also used for the ILES presented in this paper.

III. Computational Tools

A. LES Tool

The incompressible Navier–Stokes equations are discretized on Cartesian grids. A fourth-order centered spatial discretization is used for all terms except the convective terms, which are discretized using a fifth-order WENO scheme [17]. An implicit second-order-accurate finite difference scheme is used for time discretization. Locally refined grids can be employed in regions with large gradients. Multigrid iterations are used to solve the system of equations in each time step. More details can be found in Gullbrand et al. [18]. The use of Cartesian finite difference high-order techniques offers the advantages of being highly efficient and compact, allowing the use of fine grids with reasonable computational times. These advantages make the approach most suitable for LES.

B. Proper Orthogonal Decomposition and Vortex Visualization

Large eddy simulation captures the instantaneous filtered flow structure in three space dimensions. Thereby, a large amount of data is generated. Extracting the physical properties of the flow from the data is a major challenge. Common techniques focus on the time-averaged flowfields. However, time averaging removes the information related to the 3D nature of the turbulent fluctuation. Therefore, we seek to complement the mean information with statistical quantities enabling us to characterize the time-dependent 3D nature of the flow. Here, we use POD [19] to extract information from the collected data. POD was introduced to analyze turbulent data and started from the idea that only the eddies/modes containing the most kinetic energy are of interest [19]. Consequently, one seeks to project the turbulent flowfield on a vector base that maximizes the kinetic energy content for any subset of the base. It allows an accurate description of the turbulence data using only a few modes [20]. Given a vector Q containing the field variables and a vector base Φ, the POD gives

$$Q(\mathbf{x}, t) \approx Q^N(\mathbf{x}, t) = \sum_{i=1}^{N} a_i(t)\Phi_i(\mathbf{x}) \tag{3}$$

Note that the approximation Q^N of the turbulence data set Q converges to Q when $N \gg 1$. The base vectors are computed so that they satisfy the eigenvalue problem [19,20]:

$$\langle Q(\mathbf{x}, t) \cdot Q^T(\mathbf{x}, t) \rangle \Phi(\mathbf{x}) = \lambda \Phi(\mathbf{x}) \tag{4}$$

where the superscript T denotes the transpose of the vector and $\langle . \rangle$ is the time-averaging operator. It is worth noticing that the vectors Φ are the eigenvectors of the temporal autocorrelation tensor. The eigenvalue λ_i characterizes the kinetic energy content of the mode i.

For practical reasons, it is seldom possible to solve Eq. (4), because the turbulence data set is large. Restraining the analysis to a plane, a typical LES gives a dimension of Q (two velocity components at each grid point) close to $M \sim 50,000$, requiring the solution of the $M \cdot M$ eigenvalue problem. Instead, one may limit the computational costs by using Sirovich's *method of snapshots* [21]. The idea is to transform Eq. (4) into an equivalent eigenvalue problem of size $K \cdot K$, where K is the number of snapshots used to approximate the time-averaging operation $\langle . \rangle$. For more details about the use of the *method of snapshots*, the reader is referred to Smith et al [20]. We use the three-dimensional data of the three velocity components ($M \sim 3 \times 340,000$) and $K \sim 400$ snapshots to perform the POD (corresponding to $\sim$60,000 time steps, which is equivalent to some $\sim$60 flow-through times). It was noted that increasing K beyond $\sim$300 did not influence the first POD modes significantly.

The vortex cores have been visualized using criteria based on the second eigenvalue of the velocity derivative tensor proposed by Jeong and Hussain [22] (the so-called λ_2 technique). The vortex core is approximated by the region in which the second eigenvalue of the velocity tensor is negative. The λ_2 technique can be applied to the

unsteady flowfield directly or to the POD modes Φ to represent the corresponding vortical structures.

C. Geometry and Boundary Conditions

An isothermal flow at low Mach numbers in a dump combustor is studied. The geometry corresponds to an experimental test rig located at the Ecole Nationale Supérieure de Mécanique et d'Aéronautique in Poitiers, France [5,6,23]. Laser Doppler anemometry measurements were performed within the European project MOLECULES [23]. The measurements were conducted in the inlet channels and in the combustors for both reacting and nonreacting cases.

The combustor consists of two 3-m-long channels discharging into a 2-m-long combustor, presented in Fig. 1. Each channel height is 30.4×10^{-3} m. The two channels are separated by a 10×10^{-3}-m-thick splitter plate. The splitter plate ends 70.4×10^{-3} m upstream of the dump plane, with a sharp edge with an opening angle of 14 deg. The dump plane consists of two symmetric backward-facing steps for which the step height is $h = 29.9 \times 10^{-3}$ m. The depth of the geometry (in the Z direction) is 150.5×10^{-3} m. For this particular geometry, one might compute the geometric factor R relating the height of the combustor to the height of the incoming channel. R can be seen as a measure of the expansion and is commonly used to characterize the flow and reads $R = 1.84$ in the present case. We chose the lower recirculation zone (low Y values) to be shorter than or of equal length to the upper recirculation zone, giving a typical flowfield, as shown in Fig. 1.

The computational domain starts $4h$ upstream of the expansion and includes the splitter plate. It ends $16h$ downstream of the expansion. Three different depths were tested: half of the geometry $2.5h$, the full geometry $5h$, and an extended geometry $7.5h$.

Modeling of the incoming turbulence is a difficult but important task for LES computations. Steady-inflow conditions ensure a correct incoming mass flow but do not mimic many features of turbulence. However, in some cases, strong shear appears in the flow and generates some turbulence. In the present study, we test the sensitivity of the flow to different inflow conditions so that the inflow velocity profile may be written in a general form:

$$\bar{u}(\mathbf{x}, t) = U(\mathbf{x}) + U_{\text{fluct}}(\mathbf{x}, t) + U_0 B \sin(2\pi \cdot f \cdot t) \qquad (5)$$

where U denotes the time-averaged inflow velocity, U_{fluct} generates a seemingly turbulent fluctuation [24], B is an amplitude, and f is the pulsation frequency. The averaged inflow velocity was taken from LDA measurements [6,23]. To test the sensitivity to a given velocity profile change, computations were also run using a flat profile as well as the following parabolic profile: $U = U_0 \cdot (1.4 - 0.9 y_c^2)$, where y_c is a coordinate reading zero at the center of each channel and one at each wall. It is worth noticing that the parabolic profile has a higher maximum velocity than the profile obtained from the LDA data (1.4 instead of 1.27). The amplitude B was set to zero for most of the computed cases except one, in which the resulting fluctuation has the same rms as the incoming turbulence (i.e., $\sim$10% of the bulk velocity). The excitation frequency was set to $f = 100$ Hz, corresponding to $St = f \cdot h/U_0 \sim 0.26$. The resulting coherent forcing has the same amplitude as the seemingly turbulent fluctuation, but concentrates all the turbulent kinetic energy on one single frequency. It acts as mass flow modulation and resembles the effect of a strong acoustic wave, as characterized by Bruel et al. [6,23]. This frequency was chosen because it corresponds to the second longitudinal acoustic resonant mode of the test rig as measured by Bruel et al. [6,23].

The seemingly turbulent fluctuation was generated using a digital filter based approach [24]. The fluctuation term U_{fluct} is given as function of the local Reynolds stress components and the local turbulent characteristic length scales. In the present case, the Reynolds stress components were taken from the LDA measurements of Nguyen and Bruel [6,23], and the local turbulent characteristic length scales (or filter lengths) were taken from the study of channel flows by Klein et al. [24]. A mass conservative zero-gradient outflow boundary condition was used. No-slip walls were enforced without any special treatment.

The computational domain includes the whole 3D geometry. Eight different computational grids were used. Three grids covered only half of the experimental geometry. The coarser grid consists of 650,000 points, giving a mesh spacing of $\sim 2 \times 10^{-3}$ m in the expansion region. The medium-size grid contains $\sim 1,300,000$ points, with an average mesh spacing of $\sim 1.6 \times 10^{-3}$ m. Finally, the finer grid contains 2,630,000 points, with average mesh spacing of $\sim 1.3 \times 10^{-3}$ m. The wider grids (runs 8 and 9) are as fine as the medium grid but cover a larger geometry. Figure 1 shows a 2D cut of the medium grid with only every fourth point in each direction being presented. Table 1 summarizes the cases studied in the present paper. It is worth stressing that the computational geometry used for the sensitivity analysis contains only half of the real geometry. The major motivation is to reduce the CPU cost and to perform several simulations. In the following section, we also investigate the influence of the computational domain width upon the results. Note that the data used for comparison with the LDA measurements [23] and for analyzing the turbulent flow are computed using the full

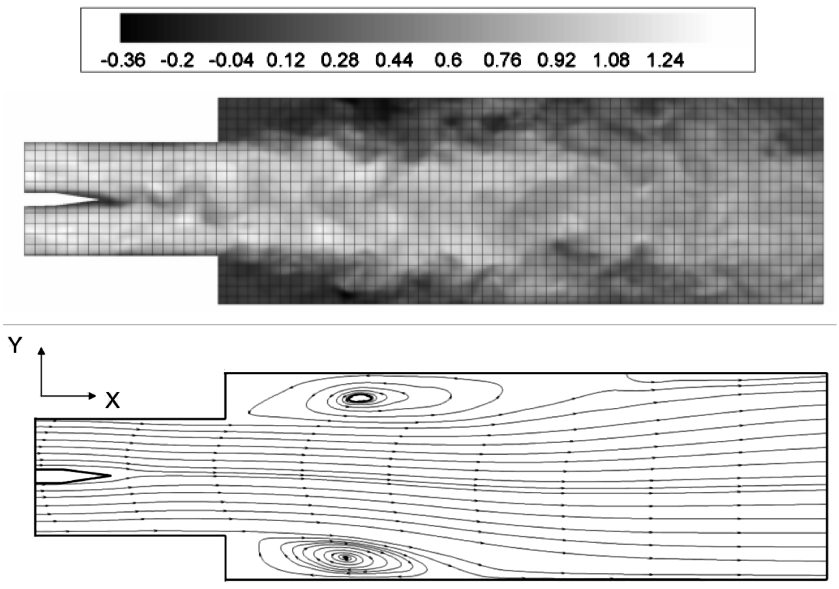

Fig. 1 Schematic X–Y cut of the channels, splitter and combustor with instantaneous streamwise velocity (top) and with streamlines corresponding to the time-averaged flowfield (bottom); numerical grid (run 8) is presented with only every four points being shown.

Table 1 Presentation of the simulations

Run No.	Grid	$U(\mathbf{x})$	U_{fluct}	B	Domain size	R	A_h
1	Medium	Fit from LDA	Fit from LDA	0	$20h \times 4.37h \times 2.5h$	1.84	2.5
2	Fine	Fit from LDA	Fit from LDA	0	$20h \times 4.37h \times 2.5h$	1.84	2.5
3	Coarse	Fit from LDA	Fit from LDA	0	$20h \times 4.37h \times 2.5h$	1.84	2.5
4	Medium	Flat profile	Fit from LDA	0	$20h \times 4.37h \times 2.5h$	1.84	2.5
5	Medium	Parabolic profile	Fit from LDA	0	$20h \times 4.37h \times 2.5h$	1.84	2.5
6	Medium	Fit from LDA	0	0	$20h \times 4.37h \times 2.5h$	1.84	2.5
7	Medium	Fit from LDA	0	$\sim 0.1 \times \sqrt{2}$	$20h \times 4.37h \times 2.5h$	1.84	2.5
8	Medium-wide	Fit from LDA	Fit from LDA	0	$20h \times 4.37h \times 5h$	1.84	5
9	Medium-wide	Fit from LDA	Fit from LDA	0	$20h \times 4.37h \times 7.5h$	1.84	7.5
10	Medium-wide	Fit from LDA	Fit from LDA	0	$20h \times 3.31h \times 5h$[a]	1.4	5[a]–10.6
11	Medium-wide	Fit from LDA	Fit from LDA	0	$30h \times 7.10h \times 5h$[a]	4	5[a]–2.1

[a]Computed using the base-case step height $h = 0.0299$ m

geometry (i.e., run 8). In addition, Table 1 also presents two runs performed with different geometries (runs 10 and 11) for investigating the sensitivity to the expansion ratio R. In both cases, the incoming channel is similar to that in the other runs, but it discharges into two different combustors such that R varies from 1.4 (run 10) to 4.0 (run 11).

The time step was determined to give a Courant–Friedrichs–Lewy (CFL) number ~ 0.4 to preserve time accuracy. The time-averaged quantities were computed over $\sim 16,000$ time steps (corresponding to ~ 16 flow-through times), except for run 8, in which $\sim 25,000$ time steps were used (corresponding to ~ 25 flow-through times). The recirculation zone length was computed as the largest distance from the step to the streamwise velocity isolevel $U = 0$. The region very close to the wall (the four nearest cells) was ignored in the determination of recirculation zone length.

The inflow bulk velocity was set to 11.5 m/s, giving Reynolds numbers of 22,200 (cases 1–9), 10,700 (case 10), or 79,000 (case 11) and a Mach number of 0.033 in all cases. The operating temperature and pressure were 293 K and 101,325 Pa, respectively. The results presented in this paper are normalized by the bulk velocity and the step heights.

IV. Results and Discussion

A. Grid Sensitivity Analysis

First, the influence of the computational-grid density on the results was investigated. We consider runs 1 to 3, as presented in Table 1.

Figure 2 shows the normalized mean streamwise velocity profiles at five different streamwise locations in the combustor. The profiles are located in the middle plane relative to the spanwise direction. At $x/h = 0$, the jet issues into the combustor. At $x/h = 1$, the profile exhibits a minimum, a result of the wake of the splitter plate. As the jet penetrates into the combustor and spreads, two recirculation zones are created. The three grids capture the mean flow pattern properly and predict a similar jet spreading rate. The three grids also predict the bending of the jet leading to the asymmetry in the profiles. Close to the expansion, the profiles look identical. Further downstream, the medium and fine grids predict a larger bending of the jet compared with the coarse grid. In addition, the medium and fine grids predict a shortened reattachment length on the lower wall and a longer reattachment length on the upper wall. The return to symmetry with increasing distance from the expansion is also earlier with the coarser grid, which can be explained by a higher numerical diffusion that affects the results.

Figure 3 shows the rms of the streamwise velocity fluctuations. The fluctuation levels predicted by the three grids are very similar both in magnitude and in shape. Close to the expansion, the three grids predict similar profiles. Further downstream, the coarse-grid results depart from the others as a consequence of the discrepancies mentioned in the previous paragraph. The medium and fine grids predict almost identical profiles, except at the location $x/h = 9$, where the fine grid predicts higher fluctuation levels in the upper part of the combustor. The difference is $\sim 20\%$ and may result from a better resolution on the fine grid. However, the differences in predictions between the medium and fine grids are small and we use the medium grid for the continuation of the study.

B. Sensitivity to the Inflow Boundary Conditions

The boundary conditions, together with adequate resolution, are a major issue in large eddy simulation. The incoming flow can be assimilated to a fully developed channel flow that convects turbulence into the computational domain. In addition, the averaged velocity profiles are not flat. In the present section, we investigate the influence of the inflow boundary conditions on the results to assess the effect of inflow uncertainty on the predicted flowfield.

Firstly, we consider the effect of the averaged velocity profile. Nguyen et al. [23] measured the velocity profiles in the channels. The LES inflow boundary conditions can be enforced so that they fit to the LDA results. We also consider two other cases: one with a parabolic profile and one with a flat profile. For these three cases, we ensured the same incoming mass flow and we supplemented the time-averaged quantities with seemingly turbulent fluctuations. Figure 4

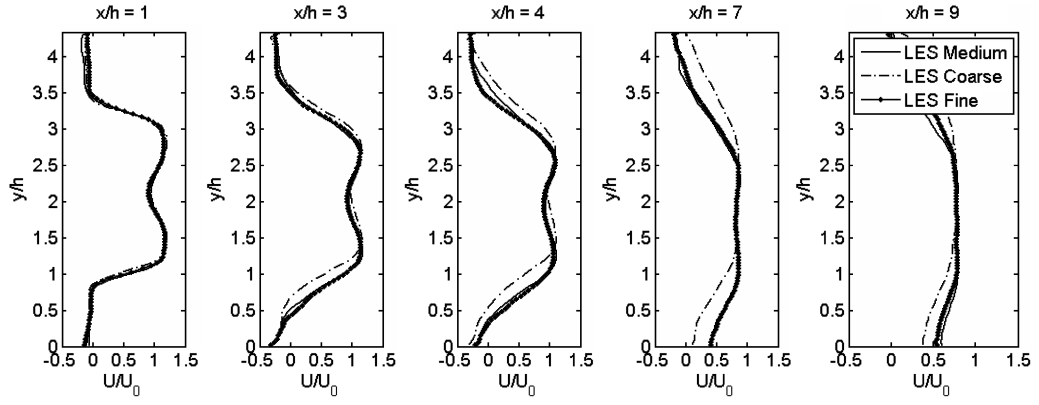

Fig. 2 Crosswise profiles of the normalized mean streamwise velocity $\langle u \rangle / U_0$ at different streamwise positions using different computational grids for runs 1–3.

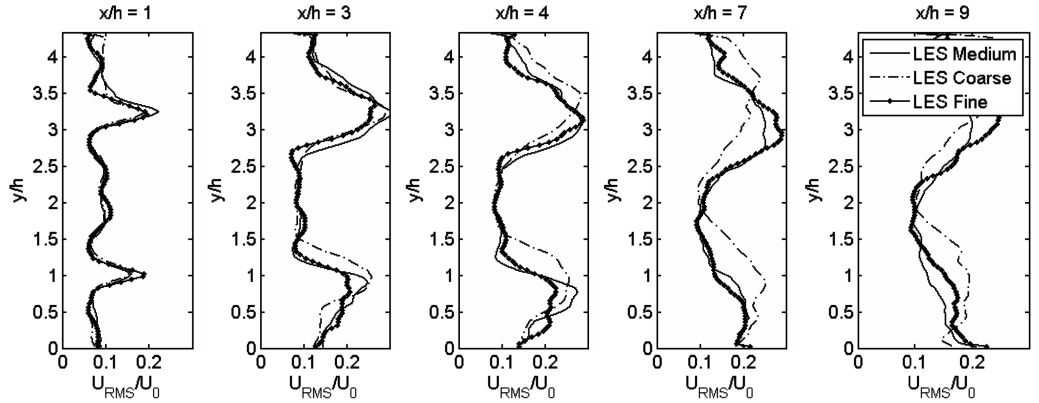

Fig. 3 Crosswise profiles of the normalized rms of the streamwise velocity fluctuation at different streamwise positions using different computational grids for runs 1–3.

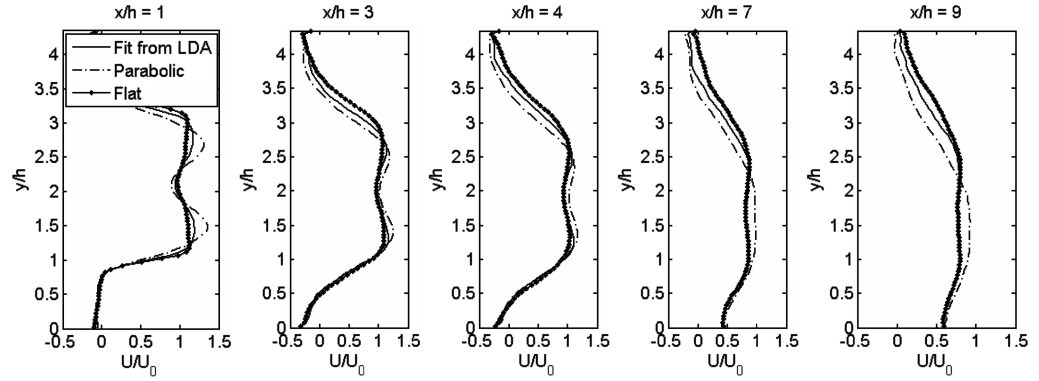

Fig. 4 Crosswise profiles of the normalized mean streamwise velocity $\langle u \rangle / U_0$ at different streamwise positions using different inflow boundary profiles for runs 1, 4, and 5.

shows the averaged streamwise velocity profiles. Close to the expansion, the profiles show a memory of the inflow boundary and reproduce qualitatively the same trend; the run with flat inflow conditions results in a relatively flat profile, whereas the run with parabolic inflow conditions gives steeper gradients. This difference vanishes further downstream. The difference is already small at $x/h \sim 3$.

Figure 5 shows the fluctuations of the streamwise velocity for the same three runs. A similar trend is observed as the difference decreases further downstream. The run with parabolic inflow conditions exhibits stronger fluctuations because the mean profiles have steeper gradients. The resulting shear-layer instabilities are stronger than in the other cases, resulting in higher rms values. However, one should stress that the tested profiles depart significantly from the LDA fit but do not result in significantly different predictions. One may conclude that the uncertainty related to the averaged inflow boundary condition is low enough to be neglected.

A second analysis considers the effect of the unsteady component of the inflow boundary. In runs 6 and 7, we change the nature of the inflow boundary condition fluctuation. In one case, the fluctuations are set to 0 (steady-inflow boundary conditions), and in the other, we replace the seemingly turbulent fluctuations by a low-frequency sinusoidal pulsation. Figure 6 shows that the effect of the seemingly turbulent fluctuations and of the periodic pulsation on the averaged profiles are significant. Regarding the low-frequency pulsation, it partially restores the symmetry of the profile so that the reattachment lengths on the upper and lower walls are almost the same. Using steady-inflow boundaries increases the bending of the jet. In addition, the profiles shown in Fig. 6 seem to suggest that a higher mass flow is injected in the pulsating case. This is not so and can be explained by the 3D features of the flow. If the pulsation restores the symmetry in the x–y plane, it also modifies the flow in the spanwise direction.

Figure 7 confirms the previous findings. At the expansion plane, the turbulence injected in the domain issues in the combustor explains why the steady-inflow case corresponds to lower fluctuations close to the dump plane. The discrepancies in the fluctuations decrease downstream of $x/h \sim 4$ due to the strong shear-layer instability. The low fluctuation levels explain why the jet bending is stronger in the steady-inflow case: the momentum transfer between the jet and the recirculation zones is lower. The changes in flow feature induced by the pulsation can also be seen in the fluctuation levels and profiles. Note that these changes decrease downstream. One may conclude that the present computations are relatively sensitive to the inflow boundary conditions, but that the flow asymmetry remains, providing that no low-frequency excitation (i.e., a relatively strong acoustic wave) is present. It is the case, because Nguyen et al. [6,23] did not report any significant acoustic fluctuation for their nonreacting experiments.

C. Comparison with Experimental Data

Sections IV.A and IV.B established the sensitivity of LES predictions to the inflow boundary conditions and established that the medium grid was suitable for performing the computations. Consequently, the results of run 8 will be chosen for comparison with the experimental data from Nguyen et al. [23]. Figure 8 shows the streamwise velocity field along lines obtained from both LDA measurements [23] and from LES. The jet discharges into the combustor. Above and below the jet, two recirculation zones are formed as the jet discharges into the combustor. From $x/h \sim 3$, one can see that the jet is deflected toward one of the walls. The jet deflection implies that the upper recirculation zone is larger than the lower zone. The flow reattaches further downstream, but the streamwise location of the reattachment is different on each side. The upper recirculation zone extends to $x/h \sim 7$, whereas the lower recirculation zone ends at $x/h \sim 5.5$. The agreement between the

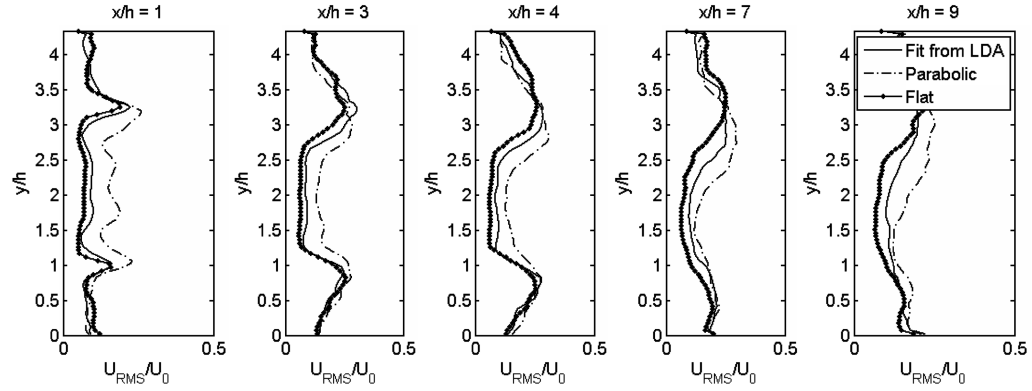

Fig. 5 Crosswise profiles of the normalized rms of the streamwise velocity fluctuation at different streamwise positions using different inflow boundary profiles for runs 1, 4, and 5.

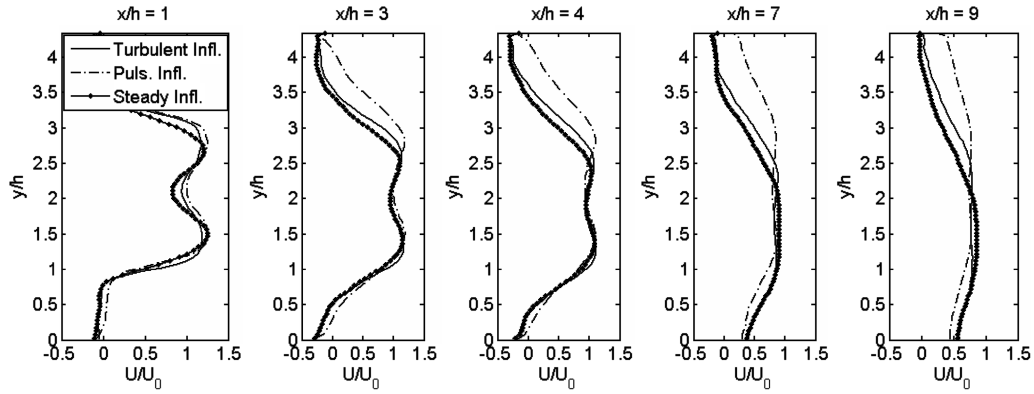

Fig. 6 Crosswise profiles of the normalized mean streamwise velocity $\langle u \rangle / U_0$ at different streamwise positions using different inflow fluctuations for runs 1, 6, and 7.

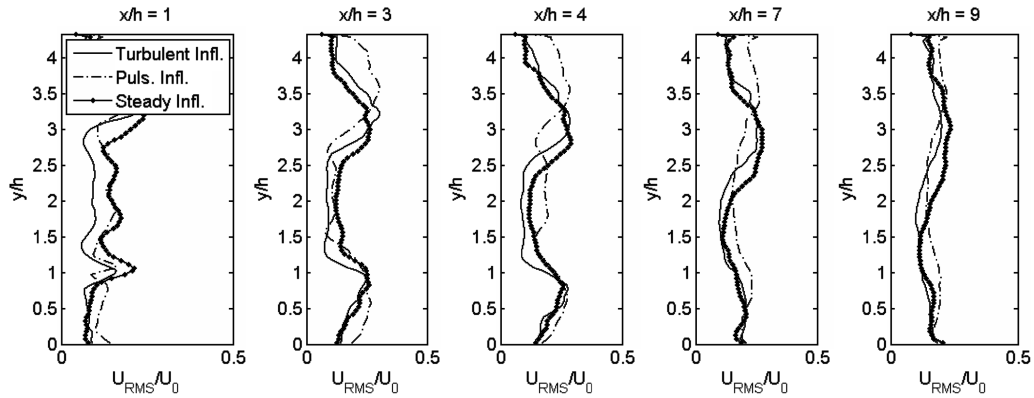

Fig. 7 Crosswise profiles of the normalized rms of the streamwise velocity fluctuation at different streamwise positions using different inflow fluctuations for runs 1, 6, and 7.

two sets of data is very good, and LES captures the jet average bending accurately, as well as the average reattachment points (i.e., lower and upper recirculation zone sizes and intensities). Small departures from the two data sets can be seen close to the expansion in the upper and lower recirculation zones, as well as at the center of the domain for $x/h > 7$. The differences are small, but above the experimental uncertainty. The LES predictions overestimate slightly the spreading of the jet at $x/h = 9$.

Figure 9 shows the rms of the streamwise velocity fluctuations. The velocity fluctuations reach a maximum in the shear layers between the central jet and the two recirculation zones. The numerical and experimental results agree well both qualitatively and quantitatively. Note that for x/h in the range [4,7], the LES overestimates the fluctuations intensity; this explains why the jet spreading rate was slightly overestimated.

Further, the crosswise velocity component statistics were investigated using both LDA measurements [23] and LES. The averaged crosswise velocity is presented in Fig. 10 and is low (in magnitude) compared with the axial component. Both the LES and LDA data show that the flow is mainly in the streamwise direction, with a slight downward deflection corresponding to the jet bending. The rms of the crosswise velocity fluctuation (Fig. 11) exhibits maxima in the shear layers. For $x/h > 6$, the agreement between LES and the LDA data is very good. Further upstream, the LES data overestimates the fluctuations along the centerline. In fact, the peak in this region corresponds to the wake of the splitter plate. Consequently,

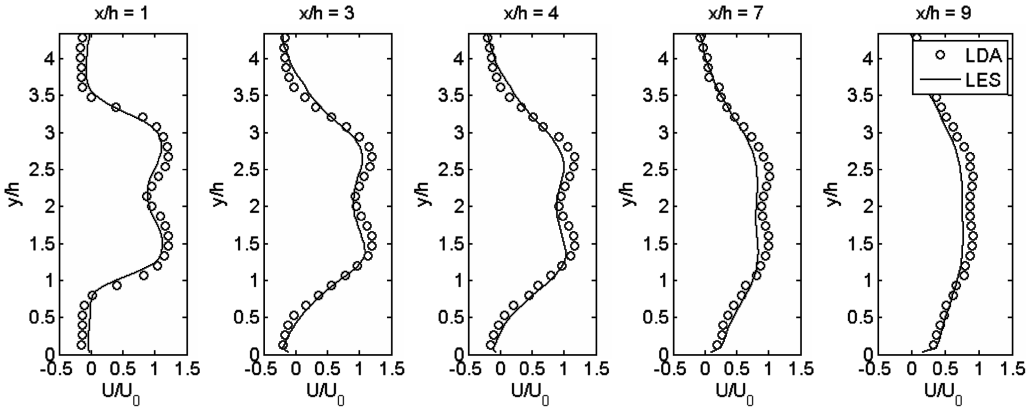

Fig. 8 Crosswise profiles of the normalized mean streamwise velocity $\langle u \rangle / U_0$ at different streamwise positions; LDA measurements [23] vs run 8.

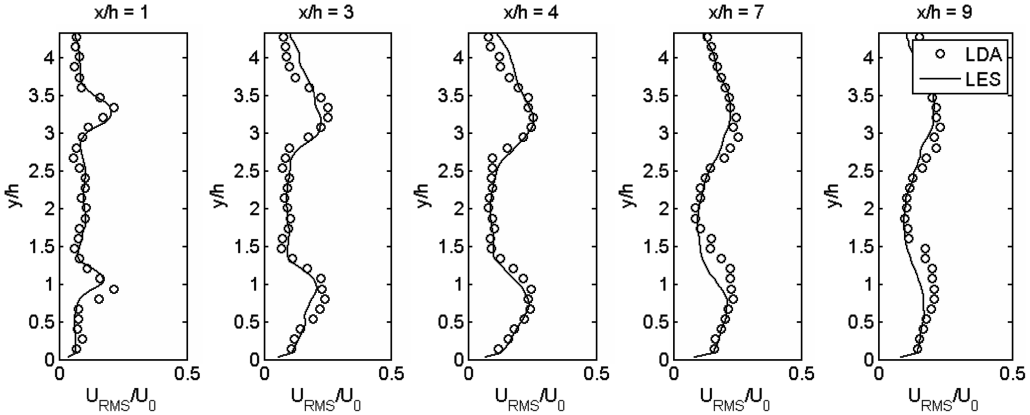

Fig. 9 Crosswise profiles of the normalized rms of the streamwise velocity fluctuations at different streamwise positions; LDA [23] measurements vs run 8.

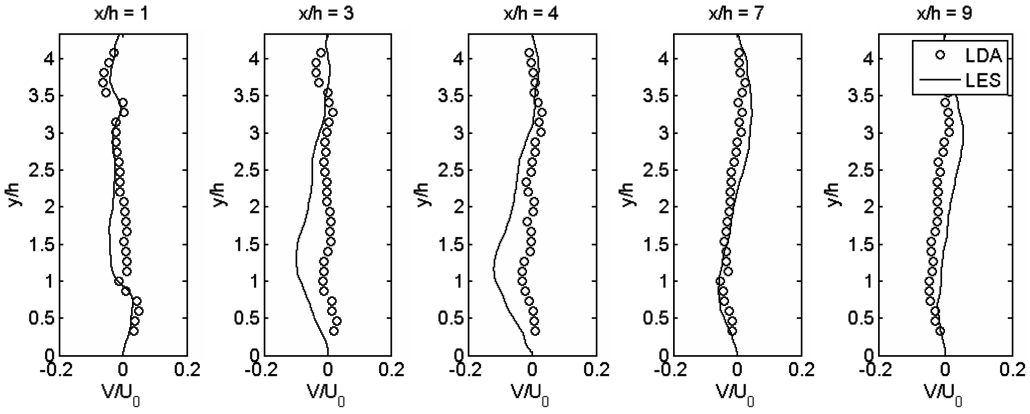

Fig. 10 Crosswise profiles of the normalized mean crosswise velocity $\langle v \rangle / U_0$ at different streamwise positions; LDA [23] measurements vs run 8.

the LES data underpredicts the decay of turbulence in the wake. Finally, the Reynolds stress R_{UV} predicted by LES is compared with LDA measurements (Fig. 12). The agreement is good, indicating that the LES tool accurately captures the turbulent transfer of momentum from the jet to the two recirculation zones. It is worth noting that both U_{rms} and R_{UV} are nonzero in the whole domain and not only in the shear layers. It indicates that the fluctuations are relatively strong in the recirculation zones, leading to a time-dependent behavior of the recirculation zones in terms of length and strength.

D. Sensitivity Channel Width

In this section, we present results from runs 8, 9, and 1 and discuss the sensitivity of the predictions to $A_h = \Delta Z/h$. Figure 13 shows the averaged streamwise velocity for the three cases. For these cases, the jet bends, creating two asymmetric outer recirculation zones behind the steps. However, the jet deflection and the recirculation zone lengths are sensitive to ΔZ. Reducing the spanwise dimension of the geometry increases the jet deflection and sharpens the velocity gradients in the shear layers. As a consequence, it lengthens the upper recirculation zone and shortens the lower zone. Figure 14 shows the rms of the streamwise velocity fluctuations for the three cases. As seen previously, the maxima lie in the regions of the shear layers. Increasing the spanwise dimension of the geometry reduces the fluctuation levels correlated to the decrease of the shear mentioned earlier. For $x/h < 4$, the rms of the streamwise velocity fluctuation decreases with ΔZ. This point is supported by the study of the time variation of the shorter recirculation length x_R presented in Fig. 15.

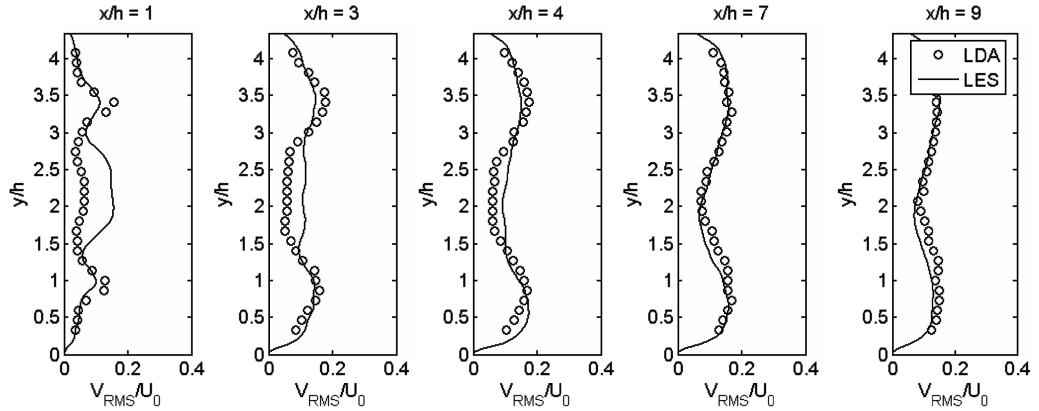

Fig. 11 Crosswise profiles of the normalized rms of the crosswise velocity fluctuations at different streamwise positions; LDA [23] measurements vs run 8.

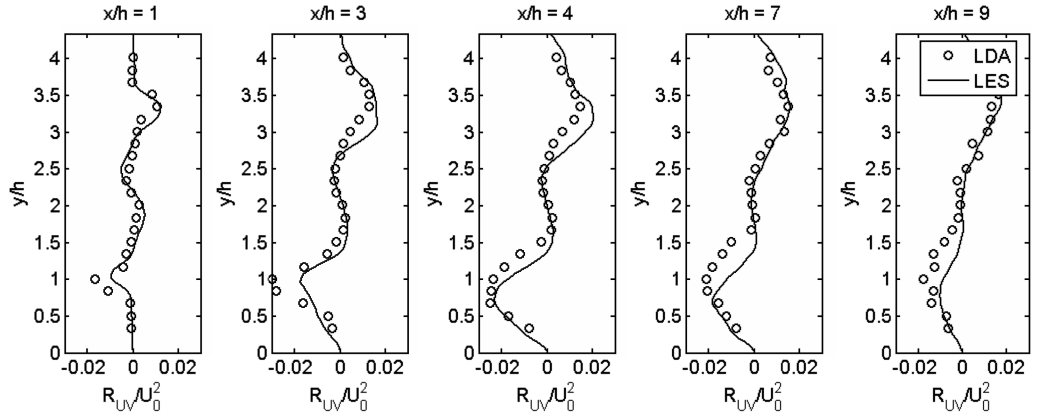

Fig. 12 Crosswise profiles of the normalized Reynolds stress component $R_{\mathrm{UV}} = (\langle uv\rangle - \langle u\rangle\langle v\rangle)/U_0^2$ at different streamwise positions; LDA [23] measurements vs run 8.

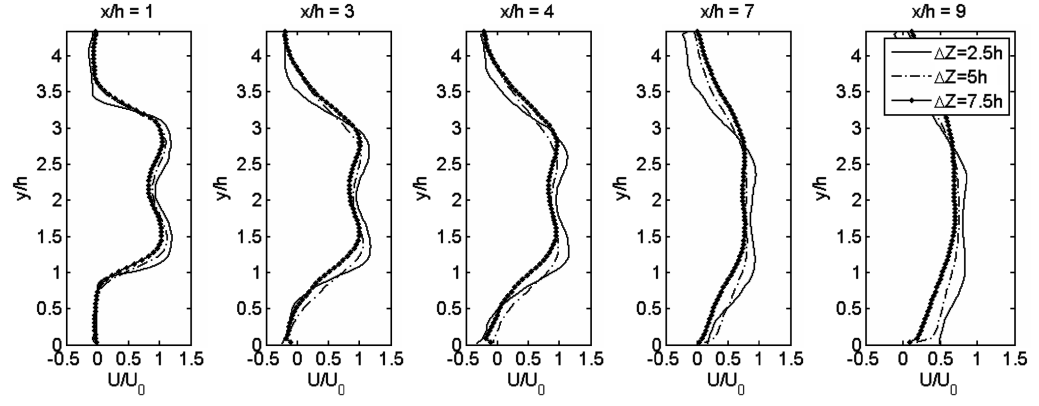

Fig. 13 Crosswise profiles of the normalized mean streamwise velocity $\langle u\rangle/U_0$ at different streamwise positions for runs 1, 8, and 9.

As previously pointed out, the jet deflection decreases with A_h so that x_R increases with A_h. The root mean square of x_R fluctuation also increases with A_h, indicating a larger turbulence level. The higher turbulence level indicates a larger momentum transfer from the jet to its surrounding and hence a lower jet deflection. One may explain the effect of the depth on the results by considering the 3D nature of turbulence. In particular, relatively thin domains will constrain the large turbulent structures in the spanwise direction. This limitation affects the turbulence, as shown in Fig. 15, and increases the jet deflection. Note that no periodic fluctuation could be identified by studying the time variation of x_R.

E. Sensitivity to the Step Height or Expansion Ratio

In this section, we test the sensitivity of the predictions to the step height/expansion ratio R. Because the geometry changes, we introduce a modified coordinate system (x^*, y^*) with $x^* = x/h$ and

$$y^* = a \cdot (y - 0.5 \cdot H_{\mathrm{comb}})^2 + b \cdot (y - 0.5 \cdot H_{\mathrm{comb}})$$

where the couple (a, b) is chosen so that $y = 0.5 \cdot H_{\mathrm{channel}}$ gives $y^* = 0.5$ and $y = h + 0.5 \cdot H_{\mathrm{channel}}$ gives $y^* = 1$. In the coordinate change, the lengths are taken from the corresponding geometries; that is, h denotes the step size varying from 0.01416 m (run 10) to

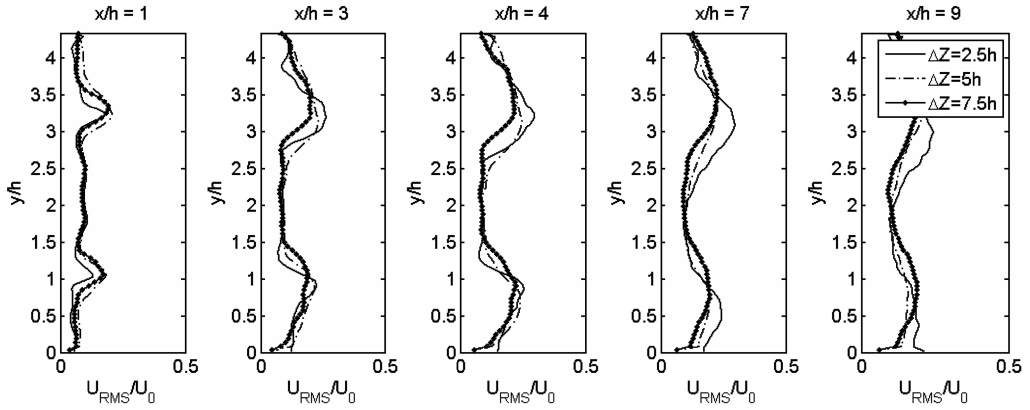

Fig. 14 Crosswise profiles of the normalized rms of the streamwise velocity fluctuations at different streamwise positions for runs 1, 8, and 9.

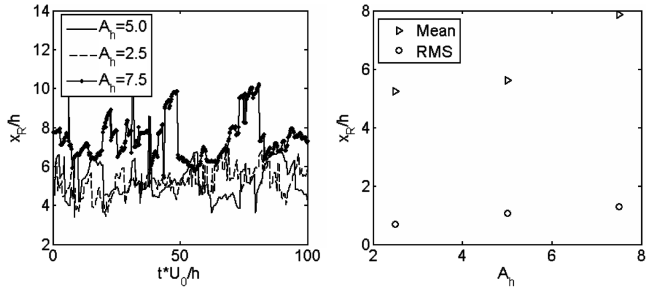

Fig. 15 Time plot of the length of the shorter recirculation zone (left) and mean and rms of the shorter recirculation zone length (right).

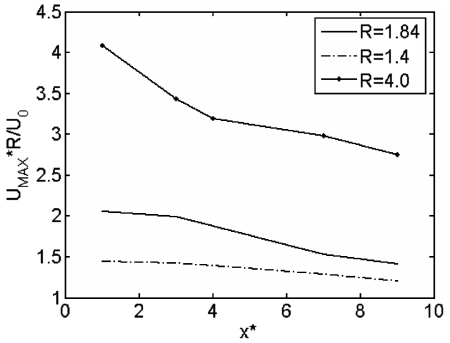

Fig. 17 Maximum streamwise velocity normalized by the combustor bulk velocity vs x^*.

0.0708 m (run 11). Within the new coordinate system, we plot the results of runs 8, 10, and 11. Figure 16 shows the averaged streamwise velocity. For $R = 1.4$, the flowfield is symmetric. The jet enters the combustor and two symmetric recirculation zones are formed behind the steps. Increasing R leads to a loss of symmetry, with the jet bending toward one of the walls. The bending angle increases with R. A consequence is that the lower recirculation zone decreases significantly in length as R increases: from $x^* \sim 7$ to ~ 3.5. The velocity profiles at $x^* = 9$ suggest that increasing R flattens the profile. However, one should remember that the bulk velocity in the combustor behaves as U_0/R. Figure 17 shows the maximum streamwise velocity normalized by U_0/R. Far downstream, one expects to recover a fully developed channel flow with a maximum $\sim 1.2U_0/R$. Figure 17 shows that it takes longer to reach the fully developed state with larger R. The maximum decrease rate is also higher for large R.

Figure 18 shows U_{rms} for the different values of R. Independently from R, the fluctuations exhibit a maximum in the shear layers between the jet and the recirculation zones. The locations of these maxima depend on the jet deflection and follow the remarks in Fig. 16. The magnitude of the fluctuations is similar for the three cases (Fig. 18). However, comparing with the combustor bulk velocity, one notices that the relative fluctuation level increases as R gets bigger. It means that the turbulent stresses are larger as R increases, because shear layers are getting stronger.

Figure 19 shows the influence of R on $x_h \cdot \langle x_h \rangle$ decreases with R as the jet bending angle increases. The rms of x_h fluctuation indicates that the fluctuations decrease with R. However, increasing R resulted in decreasing A_h which leads to a decrease of the recirculation length fluctuation, as shown in Sec. IV.D. Consequently, it does not enable us to determine the effect of R on the recirculation length fluctuation. Note that the study of the time variation of x_R did not show any periodic fluctuation.

F. Three-Dimensional Features of the Flow and Identification of Large-Scale Motions

Section IV.D described the influence of the spanwise length of the domain on the flow and turbulence field. The effect of the third

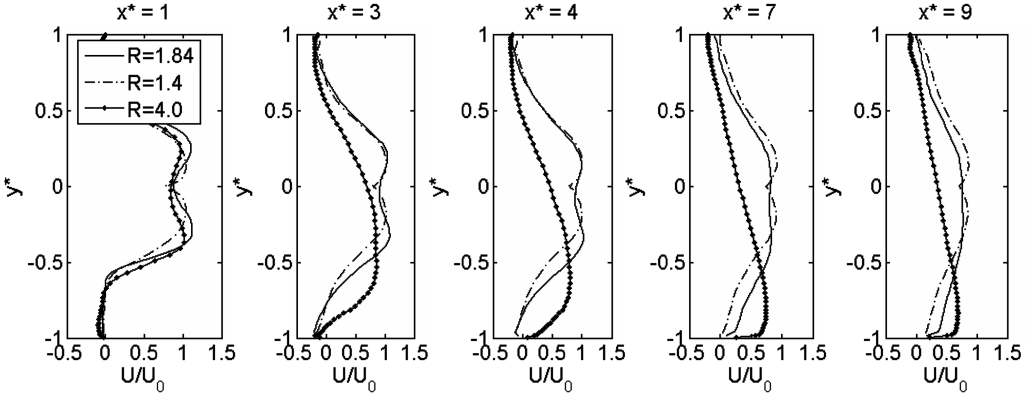

Fig. 16 Crosswise profiles of the normalized mean streamwise velocity ($\langle u \rangle / U_0$ vs y^*) at different streamwise positions for runs 8, 10, and 11.

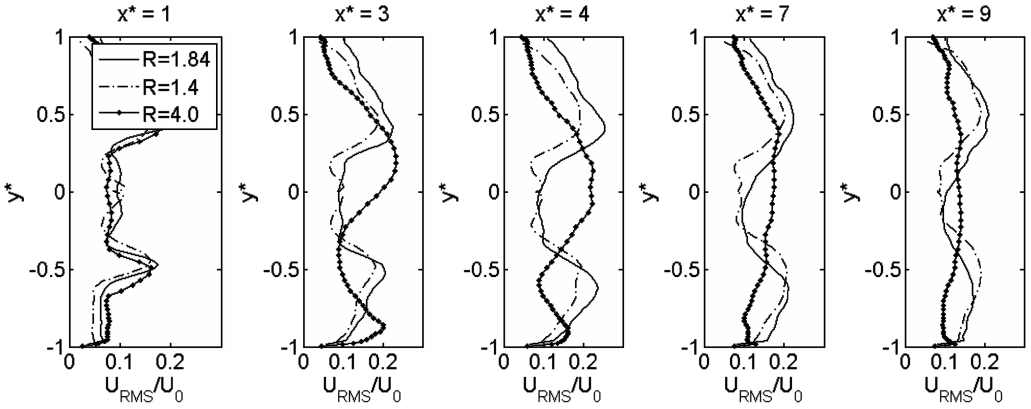

Fig. 18 Crosswise profiles of the normalized rms of the streamwise velocity fluctuations vs y^* at different streamwise positions for runs 8, 10, and 11.

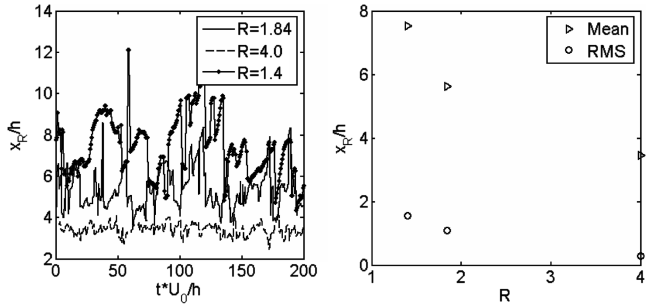

Fig. 19 Time plot of the length of the shorter recirculation zone (left) and mean and rms of the shorter recirculation zone length (right).

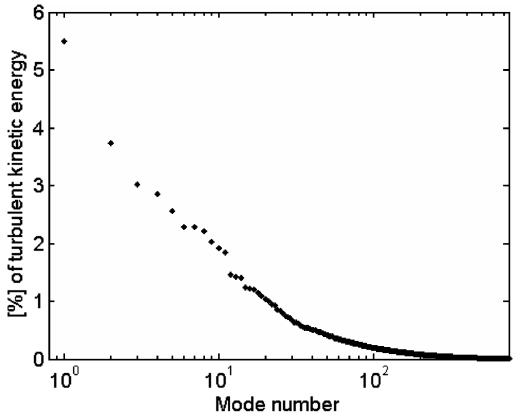

Fig. 21 Spanwise profiles of the normalized mean streamwise velocity $\langle u \rangle / U_0$ and velocity fluctuations rms at different streamwise positions for run 8.

direction is plotted in Fig. 20. The profiles of streamwise velocity and velocity fluctuations rms are flat along the spanwise direction, except close to the walls. At $z/h \sim 0$ or 5, the no-slip walls impose the streamwise velocity to be zero and the velocity gradients result in an increase of turbulence. Upstream of $x/h < 5$, the velocity profile is close to a plug flow but tends to a turbulent channel flow as one travels downstream. Note that at $x/h \sim 9$, the flow is still far from a fully developed pipe flow. However, no noticeable 3D effects are seen from the mean flow and from the fluctuation rms. Therefore, one seeks to examine statistical quantities that relate to the structure of the turbulent fluctuations and not only to the intensity: the fluctuations are decomposed into POD modes.

Figure 21 presents the distribution of the turbulent kinetic energy (TKE) among the POD modes. The distribution follows a decaying exponential distribution, with the tail extending to the mode number ~200. No dominant feature is seen from Fig. 1, with mode 1 representing only ~5.5% of the TKE (i.e., less than modes 2 and 3 together). In addition, one needs about 100 modes to recover 99% of the TKE. This result is well in line with POD analysis performed on a backward-facing step [25].

Figure 22 shows a λ_2 representation [22] of some POD modes. The fluctuation fraction depicted by mode i is presented by showing vortex tubes. No organized dominant structures are seen, but rather, a collection of small vortex tubes that are located in the shear layers and in the recirculation zones. The POD modes are not symmetric following the mean flowfield. Note that a similar conclusion was drawn by Couplet et al. [25] regarding the vortical structure of the fluctuations.

Figure 23 shows the streamwise velocity fluctuation (denoted as u') isolevel associated with the POD mode i. The isosurfaces present the spatial coherence of the fluctuation. One sees that for the four most energetic modes, the u' field covers the whole span of the combustor. As a result, the turbulent fluctuations consist of large structures that are of the size of ΔZ. It explains the trend observed in Sec. IV.D: the spanwise length of the combustor controls the size of

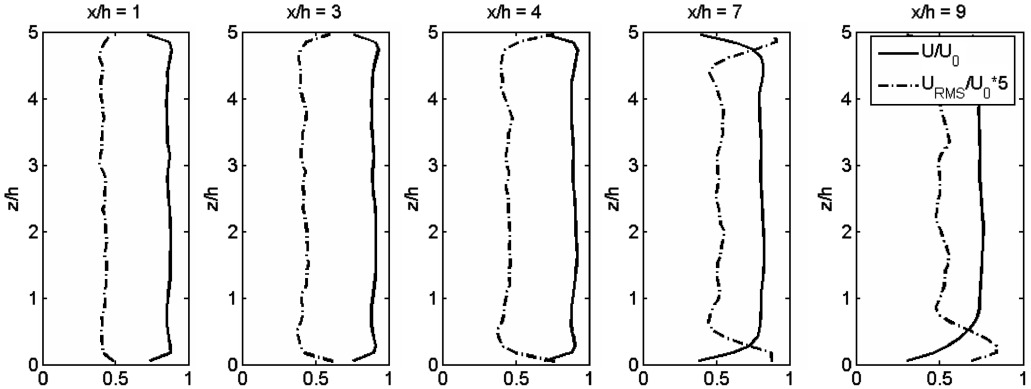

Fig. 20 Spanwise profiles of the normalized mean streamwise velocity $\langle u \rangle / U_0$ and velocity fluctuations rms at different streamwise positions for run 8.

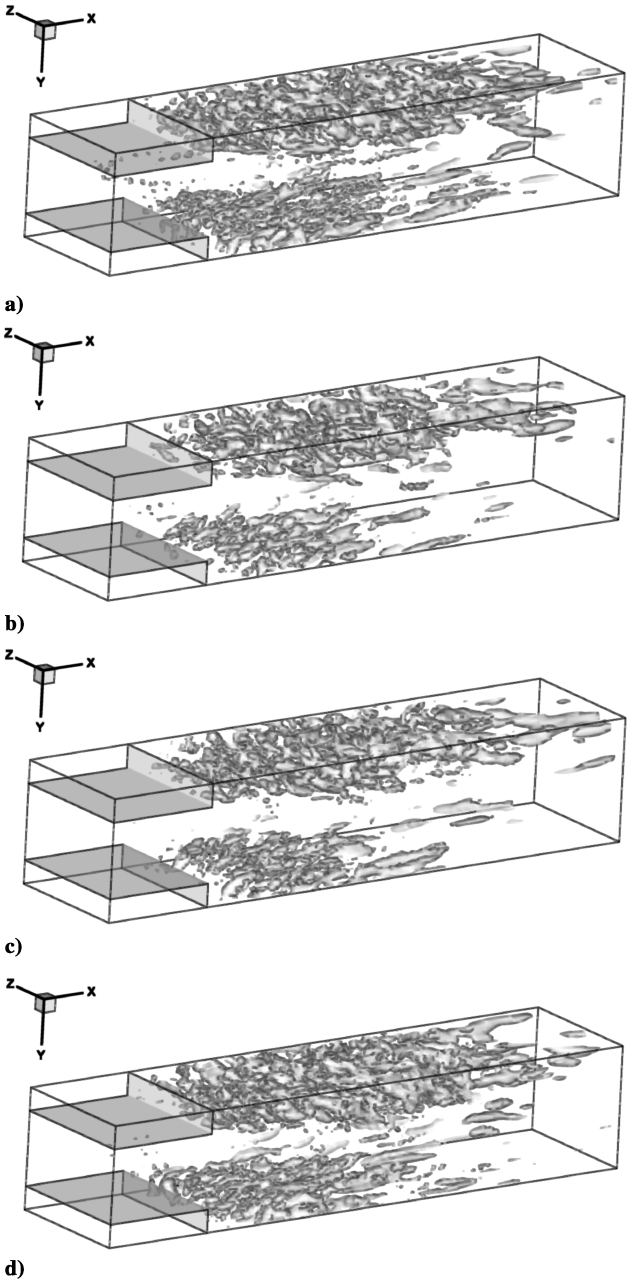

Fig. 22 Visualization of the main structures vortex core (λ_2 isosurface [22]) associated with the POD mode number i with a) $i = 1$, b) $i = 2$, c) $i = 7$, and d) $i = 9$.

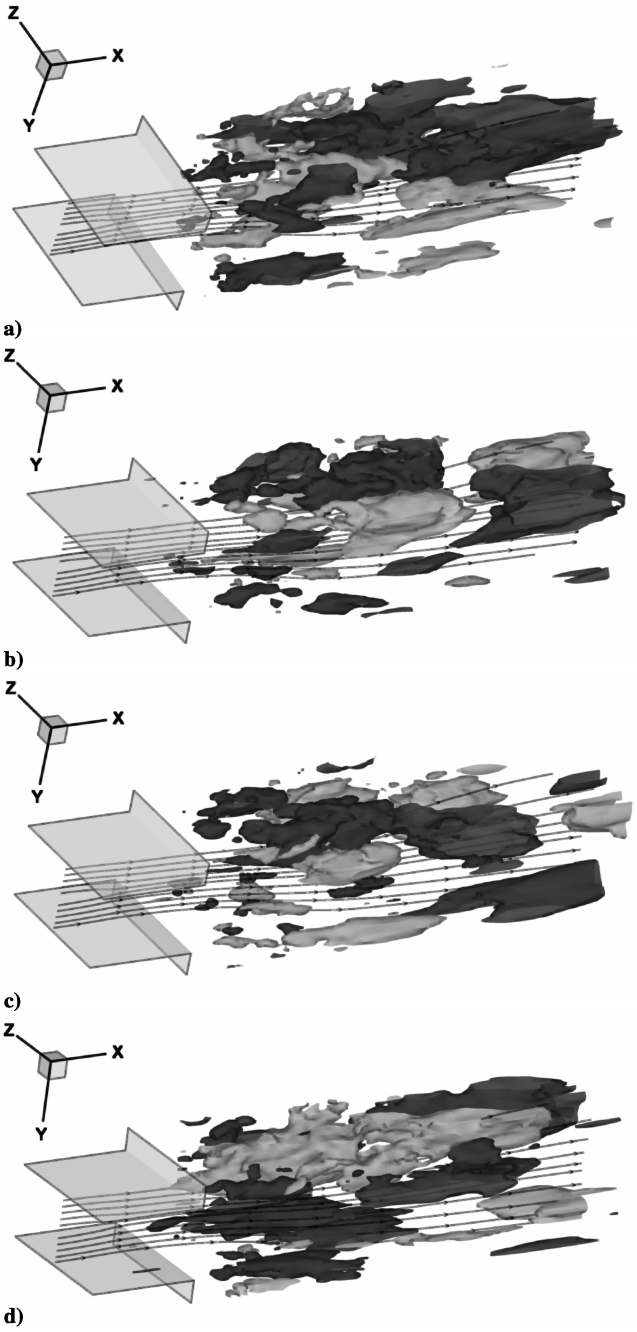

Fig. 23 Visualization of the axial velocity fluctuation $\Phi u'$ associated with the POD mode number i with a) $i = 1$, b) $i = 2$, c) $i = 3$, and d) $i = 4$; black denotes $\Phi u' > 0$ and gray denotes $\Phi u' < 0$; the streamlines depicting the average flowfield are also presented.

the turbulent structures. The larger ΔZ is, the larger are the turbulent structures that can fit into the geometry. Because large turbulent structures contain more kinetic energy than small structures, increasing ΔZ induces an increase of the turbulence level. Hence, the momentum exchange between the jet and the recirculation zone is promoted by increasing ΔZ, and the jet deflection decreases as ΔZ increases.

V. Conclusions

The paper reports a numerical investigation of a rectangular jet issuing into a larger cavity using implicit large eddy simulation (LES). The mean results were found insensitive to the numerical grid, weakly sensitive to the time-averaged inflow boundary conditions, and weakly sensitive to any realistic fluctuation (digital-filter-based technique or no fluctuation). In addition, the simulations do capture the natural symmetry breaking. The comparisons with experimental data showed a good agreement, indicating that implicit large eddy simulation is a suitable technique for simulating this type of turbulent flow. The present results suggest also that the use of steady inflow (taken from laser Doppler anemometry data) enables partially capturing the flowfield, but refinements (i.e., supplementing with realistic fluctuations) are necessary for obtaining accurate results.

Regarding the sensitivity to the geometry, the results were also found sensitive to the size of the computational domain and to the step size. In particular, reducing the depth of the combustor affected the jet bending. The proper orthogonal decomposition analysis showed that increasing the channel width allows the formation of larger turbulent structures that are more energetic and improve the momentum exchange (i.e., decrease the jet bending). Indeed, only full combustor simulations can accurately capture the flowfield, because the jet bending depends on the spanwise length of the combustor. It limits the accuracy of Reynolds-averaged Navier–Stokes techniques, in which 2D approximations of the geometry are

common. In addition, using reduced geometry in the spanwise direction (commonly used in LES for reducing computational costs) will also affect the results.

Regarding the physics of the flow, the recirculation zone lengths depend highly on the channel width and the expansion ratio. The time fluctuations of the lengths are also dependent on these parameters and increase with the channel width. This should be taken into account when designing devices: for example, when the backflows are used to stabilize flames by recirculation of burned gases. Also, the asymmetry can be suppressed using low-frequency pulsations. It opens ways for active control strategies using relatively simple actuators.

Acknowledgments

This work was supported partially by the Swedish Energy Authority (STEM) and partially by the Swedish Research Council (VR). The computations were run on LUNARC and HPC2N facilities within the allocation program SNAC. The routine for generating the seemingly turbulent inflow was generously provided by Markus Klein (Technical University of Darmstadt, Germany). The experimental data used for comparisons were collected within the European project MOLECULES (G4RD-CT-2000-0402), which granted the authorization to use the data. The authors thank Pascal Bruel (University of Pau, France) for making available these data.

References

[1] Escudier, M. P., Oliveira, P. J., and Poole, R. J., "Turbulent Flow Through a Plane Sudden Expansion of Modest Aspect Ratio," *Physics of Fluids*, Vol. 14, No. 10, 2002, pp. 3641–3654. doi:10.1063/1.1504711

[2] Abbott, D. E., and Kline, S. J., "Experimental Investigation of Subsonic Turbulent Flow over Single and Double Backward Facing Steps," *Journal of Basic Engineering*, Vol. 84, 1962, pp. 317–325.

[3] Da Zilwa, S. R. N., Khezzar, L., and Whitelaw, J. H., "Flows Through Plane Sudden-Expansions," *International Journal for Numerical Methods in Fluids*, Vol. 32, No. 3, 2000, pp. 313–329. doi:10.1002/(SICI)1097-0363(20000215)32:3<313::AID-FLD940>3.0.CO;2-B

[4] Aloui, F., and Souhar, M., "Experimental Study of Turbulent Asymmetric Flow in a Flat Duct Symmetric Sudden Expansion," *Journal of Fluids Engineering*, Vol. 122, No. 1, 2000, pp. 174–177. doi:10.1115/1.483245

[5] Besson, M., Bruel, P., Champion, J. L., and Deshaies, B., "Inert and Combusting Flows Developing over a Plane Symmetric Expansion: Experimental Analysis of the Main Flow Characteristics," AIAA Paper 99-0412, 1999.

[6] Nguyen, P. D., and Bruel, P., "Turbulent Reacting Flow in a Bump Combustor: Experimental Determination of the Influence of an Inlet Equivalence Ratio Difference on the Contribution of the Coherent and Stochastic Motions to the Velocity Field Dynamics," AIAA Paper 2003-0958, 2003.

[7] Fuchs, L., "Incompressible Vortex Flows: Non-Uniqueness and Hysteresis," *Numerical and Applied Mathematics*, IMACS Annals on Computing and Applied Mathematics, Vol. 1, No. 1, 1989, pp. 219–224.

[8] Drikakis, D., "Bifurcation Phenomena in Incompressible Sudden Expansion Flows," *Physics of Fluids*, Vol. 9, 1, 1997, pp. 76–87. doi:10.1063/1.869174

[9] Sugawara, K., Yoshikawa, H., and Ota, T., "LES of Turbulent Separated Flow and Heat Transfer in a Symmetric Expansion Plane Channel," *Journal of Fluids Engineering*, Vol. 127, No. 5, 2005, pp. 865–871. doi:10.1115/1.1988344

[10] Fureby, C., "A Fractal Flame-Wrinkling Large Eddy Simulation Model for Premixed Turbulent Combustion," *Proceedings of the Combustion Institute*, Vol. 30, No. 1, 2005, pp. 593–601. doi:10.1016/j.proci.2004.08.068

[11] Alleborn, N., Nandakumar, K., Raszillier, H., and Durst, F., "Further Contributions on the Two-Dimensional Flow in a Sudden Expansion," *Journal of Fluid Mechanics*, Vol. 330, 1997, pp. 169–188. doi:10.1017/S0022112096003382

[12] Nathan, G. J., Hill, S. J., and Luxton, R. E., "An Axisymmetric 'Fluidic' Nozzle to Generate Jet Precession," *Journal of Fluid Mechanics*, Vol. 370, 1998, pp. 347–380. doi:10.1017/S002211209800202X

[13] Fureby, C., and Grinstein, F., "Large Eddy Simulation of High-Reynolds Number Free- and Wall-Bounded Flows," *Journal of Computational Physics*, Vol. 181, No. 1, 2002, pp. 68–97. doi:10.1006/jcph.2002.7119

[14] Grinstein, F. F., and Fureby, C., "Recent Progress on MILES for High Reynolds Number Flows," *Journal of Fluids Engineering*, Vol. 124, No. 4, 2002, pp. 848–861. doi:10.1115/1.1516576

[15] Margolin, L. G., Smolarkiewicz, P. K., and Wyszgrodzki A. A, "Implicit Turbulence Modeling for High Reynolds Number flows," *Journal of Fluids Engineering*, Vol. 124, No. 4, 2002, pp. 862–867. doi:10.1115/1.1514210

[16] Duwig, C., and Fuchs, L., "Large Eddy Simulation of Vortex Breakdown/Flame Interaction," *Physics of Fluids*, Vol. 19, No. 7, 2007, Paper 075103. doi:10.1063/1.2749812

[17] Jiang G-S., and Shu C-W., "Efficient Implementation of Weighted ENO Schemes," *Journal of Computational Physics*, Vol. 126, No. 1, 1996, pp. 202–228. doi:10.1006/jcph.1996.0130

[18] Gullbrand, J., Bai, X. S., and Fuchs, L., "High-Order Cartesian Grid Method for Calculation of Incompressible Turbulent Flows," *International Journal for Numerical Methods in Fluids*, Vol. 36, No. 6, 2001, pp. 687–709. doi:10.1002/fld.152

[19] Berkooz, G., Holmes, P., and Lumley, J. L., "The Proper Orthogonal Decomposition in the Analysis of Turbulent Flows," *Annual Review of Fluid Mechanics*, Vol. 25, 1993, pp. 539–575. doi:10.1146/annurev.fl.25.010193.002543

[20] Smith, T., Moehlis, J., and Holmes, P., "Low-Dimensional Modeling of Turbulence Using the Proper Orthogonal Decomposition: A Tutorial," *Nonlinear Dynamics*, Vol. 41, Nos. 1–3, 2005, pp. 275–307. doi:10.1007/s11071-005-2823-y

[21] Sirovich, L., "Turbulence and the Dynamics of Coherent Structures, Part 1: Coherent Structures," *Quarterly of Applied Mathematics*, Vol. 45, No. 3, 1987, pp. 561–571.

[22] Jeong, J., and Hussain, F., "On the Identification of a Vortex," *Journal of Fluid Mechanics*, Vol. 285, 1995, pp. 69–94. doi:10.1017/S0022112095000462

[23] Nguyen, P. D., Bruel, P., and Reichstadt, S., "An Experimental Database for Benchmarking Simulations of Turbulent Premixed Reacting Flows: Lean Extinction Limits and Velocity Field Measurements in a Dump Combustor," *Flow, Turbulence and Combustion* (submitted for publication).

[24] Klein, M., Sadiki, A., and Janicka J., "A Digital Filter Based Generation of Inflow Data for Spatially Developing Direct Numerical or Large Eddy Simulations," *Journal of Computational Physics*, Vol. 186, No. 2, 2003, p. 652. doi:10.1016/S0021-9991(03)00090-1

[25] Couplet, M., Basdevant, C., and Sagaut, P., "Calibrated Reduced-Order Pod-Galerkin System for Fluid Flow Modelling," *Journal of Computational Physics*, Vol. 207, No. 1, 2005, pp. 192–220. doi:10.1016/j.jcp.2005.01.008

P. Givi
Associate Editor